EXTENDED PDF FORMAT
SPONSORED BY
usb
www.usbweb.com

Science
AAAS

**Phase Diagram of Degenerate Exciton Systems**

C. W. Lai, *et al.*

*Science* **303**, 503 (2004);
DOI: 10.1126/science.1092691

***The following resources related to this article are available online at www.sciencemag.org (this information is current as of January 8, 2008 ):***

**Updated information and services,** including high-resolution figures, can be found in the online version of this article at:
http://www.sciencemag.org/cgi/content/full/303/5657/503

**Supporting Online Material** can be found at:
http://www.sciencemag.org/cgi/content/full/303/5657/503/DC1

This article has been **cited by** 22 article(s) on the ISI Web of Science.

This article appears in the following **subject collections**:
Physics
http://www.sciencemag.org/cgi/collection/physics

Information about obtaining **reprints** of this article or about obtaining **permission to reproduce this article** in whole or in part can be found at:
http://www.sciencemag.org/about/permissions.dtl

Downloaded from www.sciencemag.org on January 8, 2008

*Science* (print ISSN 0036-8075; online ISSN 1095-9203) is published weekly, except the last week in December, by the American Association for the Advancement of Science, 1200 New York Avenue NW, Washington, DC 20005. Copyright 2004 by the American Association for the Advancement of Science; all rights reserved. The title *Science* is a registered trademark of AAAS.

32. S. D. Van Dyk, W. Li, A. V. Filippenko, *Publ. Astron. Soc. Pac.* **115**, 448 (2003).
33. O. R. Pols, C. A. Tout, P. P. Eggleton, Z. Han, *Mon. Not. R. Astron. Soc.* **274**, 964 (1995).
34. A. M. N. Ferguson, J. S. Gallagher, R. F. G. Wyse, *Astron. J.* **116**, 673 (1998).
35. A. Heger, N. Langer, *Astrophys. J.* **544**, 1016 (2000).
36. G. Meynet, A. Maeder, *Astron. Astrophys.* **361**, 101 (2000).
37. W. L. Freedman *et al.*, *Astrophys. J.* **553**, 47 (2001).
38. R. B. Tully, R. J. Fisher, *Catalogue of Nearby Galaxies* (Cambridge Univ. Press, Cambridge, 1988).
39. G. Theureau *et al.*, *Astron. Astrophys. Suppl. Ser.* **130**, 333 (1998).
40. Data from Lyon-Meudon Extragalactic database, available online at http://leda.univ-lyon1.fr.
41. J. L. Tonry, J. P. Blakeslee, A. E. Ajhar, A. Dressler, *Astrophys. J.* **530**, 625 (2000).
42. R. Rozanski, M. Rowan-Robinson, *Mon. Not. R. Astron. Soc.* **271**, 530 (1994).
43. J. Belley, J. R. Roy, *Astrophys. J. Suppl. Ser.* **78**, 61 (1992).
44. Observations were made with the NASA/European Space Agency HST and obtained from the data archive at the Space Telescope Science Institute, which is operated by the Association of Universities for Research in Astronomy, under NASA contract NAS 5-26555. These observations are associated with program GO9733. This work is also based on observations obtained with the Gemini Telescope. We acknowledge the support given by ASTROVIRTEL, a project funded by the European Commission under FP5 contract no. HPRI-CT-1999-00081. J.R.M., M.A.H., and S.J.S. thank Particle Physics and Astronomy Research Council for financial support, and S.M. acknowledges the "Physics of Type Ia SNe" Research Training Network under contract HPRN-CT-2002-00303. We thank B. Januszewski for help in coordinating and executing the HST observations and P. Meikle and R. Kotak for assistance, advice, and reading of the manuscript.

**Supporting Online Material**
www.sciencemag.org/cgi/content/full/303/5657/499/DC1
SOM Text
Figs. S1 to S4
References

27 October 2003; accepted 19 December 2003

# Phase Diagram of Degenerate Exciton Systems

**C. W. Lai,[1,3]* J. Zoch,[2] A. C. Gossard,[4] D. S. Chemla[1,2,3]**

**Degenerate exciton systems have been produced in quasi–two-dimensional confined areas in semiconductor coupled quantum well structures. We observed contractions of clouds containing tens of thousands of excitons within areas as small as (10 μm)$^2$ near 10 kelvin. The spatial and energy distributions of optically active excitons were determined by measuring photoluminescence as a function of temperature and laser excitation and were used as thermodynamic quantities to construct the phase diagram of the exciton system, which demonstrates the existence of distinct phases. Understanding the formation mechanisms of these degenerate exciton systems can open new opportunities for the realization of Bose-Einstein condensation in the solid state.**

Over the last few years, the demonstration of Bose-Einstein condensation (BEC) in several atomic species confined in optical or magnetic traps has triggered intense interest (*1*, *2*). A variety of quasi-particles with bosonic character are also found in condensed matter. In particular, semiconductors can sustain bound electron-hole (e-h) pairs, called excitons. Excitons (Xs) have small effective mass (on the order of the free electron mass) and behave as bosons in the dilute limit. Theoretical work (*3*–*5*) suggests that Xs can undergo BEC at a critical temperature $T_c \approx 1$ K, a factor of $10^6$ that for atoms. However, BEC of excitons has not been established experimentally. The realization of excitonic BEC in semiconductors will open new opportunities in the manipulation of macroscopic quantum coherence because of the greater flexibilities and well-developed technology of semiconductor materials (*6*).

From a fundamental viewpoint, Xs are spatially extended (Bohr radius: $a_X \approx 10$ to 50 nm) composite particles made of loosely bound fermions that evolve not in the real vacuum but in an extremely dense ($\sim 10^{23}$ particles per cm$^3$) solid matrix. The X density, $n_X$, can be widely varied with the photoexcitation, and when $n_X$ approaches the level where the interparticle spacing becomes comparable to $a_X$, a crossover from Bose to Fermi statistics occurs. At sufficiently high densities, screening of the e-h coulomb attraction prevents the binding of e-h pairs, and the insulating X gas undergoes a Mott transition to a conducting e-h plasma (*7*). In some semiconductors, a gas-liquid phase transition can also occur where the X gas condenses into an e-h liquid (*3*–*5*, *8*, *9*).

The crucial issue from a practical viewpoint is the realization of cold, statistically degenerate X systems. Because Xs are quasiparticles of excited semiconductors with a finite lifetime, this requires Xs to cool down by emitting phonons and to reach quasi-equilibrium in a time much shorter than their lifetimes. In semiconductor coupled quantum wells (CQWs) under a static electric field perpendicular to the QW plane ($Z$ direction), the ground state is spatially an indirect X with the electron confined in one QW and the hole in the other (*10*, *11*). This separation reduces the electron and hole wave function overlap, which results in an increased radiative lifetime that in our GaAs/AlGaAs CQWs samples is about two orders of magnitude that of the direct X (e-h pairs in the same QW) (*11*). The CQWs are embedded in a three-dimensional (3D) structure resulting in relaxation of the momentum conservation along $Z$; therefore, cooling to the lattice temperature by the emission of bulk longitudinal acoustic phonons is about 3 orders of magnitude faster for Xs in GaAs QWs than for that in the bulk (*12*). Finally, the e-h spatial separation gives rise to a repulsive dipolar X-X interaction that effectively screens the in-plane disorder potential (*13*).

The quasi–two-dimensional nature (quasi-2D) of CQWs raises important theoretical issues related to phase transitions in reduced dimensionality. BEC only occurs at $T = 0$ in a homogeneous 2D system of ideal bosons (*14*, *15*) but can occur at finite $T$ when they are confined in 2D traps (*16*, *17*). Hence, producing local confined cold X systems may be a key step to realizing excitonic BEC. In that respect, applying the $T_c$ formulae for ideal bosons in a square 2D box (*17*) to the confined Xs observed in GaAs/AlGaAs CQWs gives $T_c \approx 1$ K for reachable experimental conditions.

We studied $n^+$-$i$-$n^+$ GaAs/AlGaAs CQWs composed of two 8-nm GaAs wells separated by a 4-nm $Al_{0.33}Ga_{0.67}As$ barrier (*18*). Collection of cold, dense indirect-X systems confined within localized areas of CQW samples was reported (*19*). Formation of photoluminescence (PL) ring patterns around localized excitation spots was also observed in CQW (*20*, *21*). We present here a study of the phase diagram and clarify the formation mechanisms of X systems confined in localities, which, for brevity, we continue to refer to as "traps." For the phase diagram, the thermodynamic quantities are the spatial and energy distributions (including emission energies and linewidths) of the optically active indirect Xs, measured with diffraction limit resolution by PL as a function of temperature ($T$) and laser excitation ($P_{laser}$). The phase diagram displays distinct regimes with one, in particular, that corresponds to the concentration of tens of thousands Xs in small areas ($\sim$10 μm)$^2$, at low temperature and moderate excitation. Our investigations imply that the observed X degenerate systems are not caused by condensation of Xs preexisting in the CQW structure, but that indirect Xs are formed

[1]Applied Science and Technology, [2]Physics Department, University of California at Berkeley, Berkeley, CA 94720, USA. [3]Materials Sciences Division, Lawrence Berkeley National Laboratory, Berkeley, CA 94720, USA. [4]Department of Electrical and Computer Engineering, University of California at Santa Barbara, Santa Barbara, CA 93106, USA.

*To whom correspondence should be addressed. E-mail: celai@lbl.gov

Downloaded from www.sciencemag.org on January 8, 2008

in the immediate vicinity of the traps through the distinct photoassisted capture and injection of electrons and holes.

The PL images of the indirect-X cloud for three temperatures $T = 1.7$ K, 8 K, and 20 K (Fig. 1A) at a low and uniform laser excitation power, $P_{laser} = 50$ μW, show that contraction of the X cloud is evident with decreasing bath temperature: The cloud radius decreases more than an order of magnitude to ~10 μm, whereas the peak intensity increases by a factor of 50. The 2D PL images at $T = 1.7$ K (Fig. 1B) for three $P_{laser}$ values shows that with increasing $P_{laser}$, the X cloud first contracts and then expands, exhibiting an annular shape with a darker central region that also shrinks and then expands with $P_{laser}$. The color bar scale on the figure shows the local density of Xs estimated from the PL intensity by the methods described below. From these images, we deduce the integrated PL intensity ($I_{PL}$), the root-mean-square radius ($\sigma_{PL}$), the skewedness (asymmetricity), and kurtosis ($K_{PL}$—concentration of high peaks as compared with a Gaussian distribution). These parameters are used as thermodynamic quantities to characterize the X fluid.

The phase diagram of $\sigma_{PL}(T, P_{laser})$ is shown in Fig. 2A. At either high temperature or low excitation intensity the X cloud is extended, whereas both low temperature and significant excitation are required for concentration of Xs in a small area. Indeed, $\sigma_{PL}$ is at its minimum (~10 μm) for $T < 4$ K and moderate excitation ($P_{laser} \approx 35$ μW to 500 μW). In that range, the kurtosis phase diagram $K_{PL}(T, P_{laser})$ (fig. S1) demonstrates that the X distribution is more concentrated than a Gaussian, despite the central intensity dip. It is noteworthy that $\sigma_{PL}$ exhibits steepest variations in a narrow domain—nearly vertical for $P_{laser} \leq 20$ μW and diagonal for $P_{laser} \geq 20$ μW around $\sigma_{PL} = 30$ μm, which reveals the existence of distinct phases. At fixed $T \leq 10$ K, as $P_{laser}$ is increased, the X cloud first contracts when $P_{laser}$ crosses ~20 μW, plateaus over a small range of moderate intensities, then expands. At fixed $P_{laser}$, as $T$ decreases, the X cloud contracts and experiences a sharp reduction in size near $T = 10$ K. This behavior is seen more clearly in $T$-dependent cuts of $\sigma_{PL}$ for five $P_{laser}$ values between 25 μW and 6 mW (Fig. 2B). For $P_{laser} = 25$ μW, $\sigma_{PL}(T)$ exhibits a clear kink near $T = 10$ K that confirms the sudden cloud contraction. However, that kink becomes less pronounced at higher $P_{laser}$ as $\sigma_{PL}$ becomes progressively $T$ independent. This transition is further supported by the corresponding normalized $I_{PL}(T)$ curves (Fig. 2C), which, at low excitation, have a strong $T$ dependence with an almost steplike increase between $T = 15$ K and 10 K. As the excitation density increases, the magnitude of $I_{PL}(T)$ increases by a factor of 100 but its $T$ dependence becomes progressively flatter.

The PL intensity is only sensitive to the radiative recombination of optically active, bound or unbound e-h pairs with center of mass momentum $K \approx 0$ (*22*, *23*). It may not reflect the X density, which, for CQW Xs, is more directly related to the PL peak energy ($E_0$) blue shift due to the indirect-X interaction (*24*). Therefore, to better characterize the energy distribution of the indirect-X systems, we used the PL scans that provide local spectroscopic information with a $\Delta y \approx 1.7$ μm spatial resolution (Fig. 3A). In Fig. 3B, the black curve gives the indirect-X PL intensity profile, $I_{PL,S}(y)$ (spectrally integrated over the indirect-X peak), for $P_{laser} = 200$ μW and $T = 1.7$ K. Consistent with the annular structure of the Fig. 1B images, $I_{PL,S}(y)$ exhibits a central dip surrounded by two intense maxima. The $E_0$ profile (magenta curve) shows that the blue shift increases monotonically from the cloud edges to a maximum at the center. Thus, the indirect Xs at the cloud center are dense but hot ($K > 0$), not as optically active as those cold ($K \approx 0$) ones in the bright annulus. This is consistent with the variations of the PL linewidth $\Delta E(y)$ (red curve), which narrows sharply where $I_{PL,S}(y)$ is maximal and broadens a little at the center. This behavior is observed in the region where the indirect-X cloud is concentrated. But for lower $P_{laser}$ (less than about 100 μW), the $E_0$ profile reported previously (*19*) first appears, and then, near the center, $E_0$ gradually flattens.

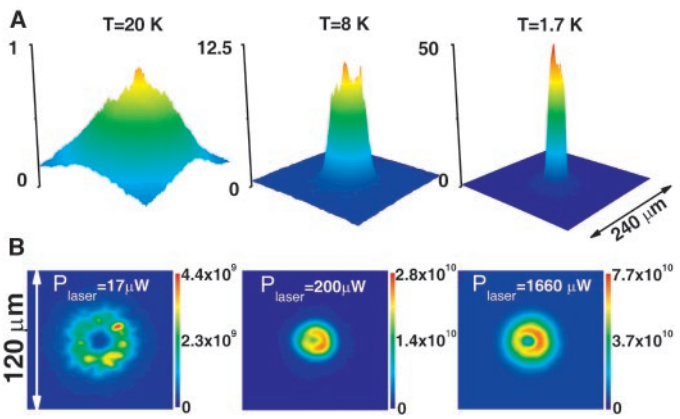


**Fig. 1.** Photoluminescence as a function of temperature ($T$) and laser excitation ($P_{laser}$) in selected images (see movie S1). (**A**) $T$-dependent PL 3D false-color images of the confined excitons (Xs) at $T = 1.7$ K, 8 K, and 20 K with $P_{laser} = 50$ μW (laser excitation spot size ~700 μm). PL intensities are rescaled as indicated on the vertical axis. The $\sigma_{PL}$ deduced from the spatial distributions are $\sigma_{PL} = 47$, 21, and 10 μm, respectively, and the $K_{PL} = -0.45$, 0.03, and +1.19, which show that the X cloud is spatially more peaked than a Gaussian. (**B**) $P_{laser}$-dependent PL 2D false-color images of confined Xs at $T = 1.7$ K for $P_{laser}$ as indicated. The estimated optically active X density is represented as a color bar. From left to right, $\sigma_{PL}$ are 19, 9, and 13 μm, respectively, and $K_{PL}$ are +0.33, +1.47, and +1.20.

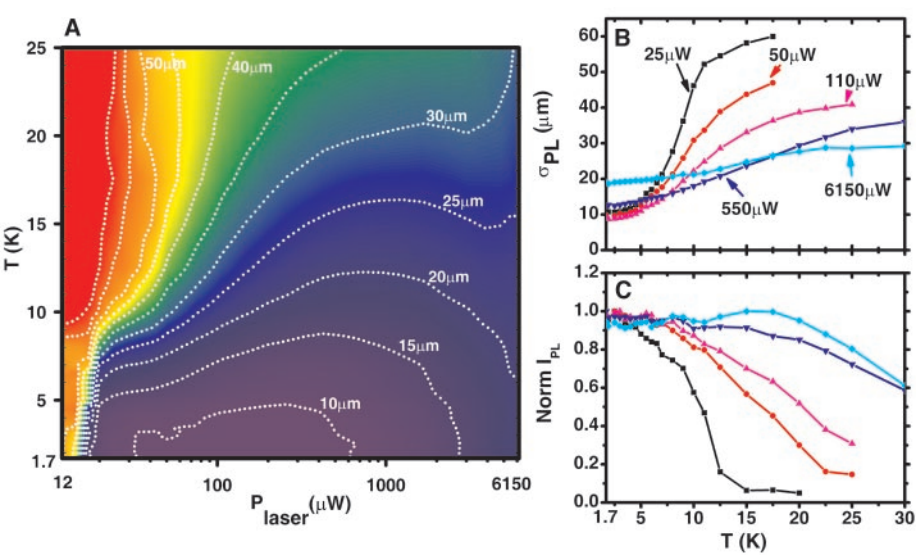


**Fig. 2.** (**A**) Full phase diagram of the root-mean-square radius of X cloud, $\sigma_{PL}(T, P_{laser})$. The white contour lines highlight the cloud extension from 10 μm to 60 μm in 5-μm steps. (**B**) Cross sections, $\sigma_{PL}(T)$, of the Fig. 2A phase diagram for fixed laser excitation intensities, for $P_{laser}$ as indicated. (**C**) $T$-dependent normalized spatially integrated PL [$I_{PL}(T)$]. $I_{PL}(T)$ rises sharply below $T \approx 10$ K for low $P_{laser}$.

Downloaded from www.sciencemag.org on January 8, 2008

The $I_{PL,S}(y)$ mean square radius, $\sigma_{PL,S}$, and the PL linewidths at the two minima, $\Delta E_{min}$, are plotted versus $P_{laser}$ (Fig. 3C) for $T = 1.7$ K. The $\sigma_{PL,S}(P_{laser})$ curve agrees with the behavior seen in Fig. 2A, i.e., the X cloud contracts to a small area, $\sigma_{PL,S} \approx 7$ μm, at low $T$ for moderate $P_{laser}$. Interestingly, the linewidth $\Delta E_{min}(P_{laser})$ curves show a parallel variation versus $P_{laser}$. At low $T$, where phonons are scarce, the low-density PL linewidth in a QW is dominated by disorder-related inhomogeneous broadening and is roughly constant, then it usually increases with the density due to the X-X interaction, X-carrier scattering, and screening. In the case of indirect Xs, however, the repulsive dipole-dipole interaction screens the in-plane potential fluctuations, an effect particularly pronounced in the statistically degenerate regime (*13*). Figure 3C reveals three regimes: (I) 20 μW $\leq P_{laser} \leq$ 100 μW, (II) 100 μW $\leq P_{laser} \leq$ 500 μW, and (III) 500 μW $\leq P_{laser}$. In regimes I and II, the indirect-X PL peak is narrow ($\Delta E < 2$ meV), although it broadens a little near the center (see Fig. 3B). This narrow linewidth confirms the well-defined X distribution. In regime III, the PL spectra near the center have significantly broad indirect-X peaks and stronger high-energy emissions, indicative of the presence of e-h plasmas. To estimate the density of Xs we combine two methods: measurements of the PL peak blue shift and careful measurements and calibration of the photon collection efficiency of the PL imaging system. The densities corresponding to the crossover between these regimes indicated by the arrows in Fig. 3C are, respectively, $n_X \approx 1.7 \times 10^{10}$ cm$^{-2}$ and $n_X \approx 4.6 \times 10^{10}$ cm$^{-2}$, still below the Mott density (*7*, *25*), $n_{Mott} \approx 10^{11}$ cm$^{-2}$ estimated from $a_X$ (*26*, *27*). Regime I corresponds to a dilute X system, whereas regime III is a hybrid X/e-h phase, where Xs may not be well defined and the effects of Fermi statistics cannot be neglected. In regime II, however, simultaneously the linewidth is the narrowest and the X cloud is the most concentrated with size depending moderately on $P_{laser}$. There the number of Xs in the X cloud varies as between about $10^4$ and $10^5$, which indicates a highly statistically degenerate phase (*19*). Thus, a dense and cold X fluid forms in regime II where the environmental fluctuations are smoothed out and the effects of scattering reduced or even suppressed.

To better understand the X collection mechanisms, we first characterized the sample under zero applied electric fields (Fig. 4A), where the PL of direct Xs dominates and the localized indirect-X cloud disappears. Molecular beam epitaxially grown QW structures have typical thickness fluctuations on the order of one monolayer, corresponding to about a 0.5-meV energy variation for our 8-nm QWs. The direct-X PL peak has a constant energy across the trap within our 0.1 meV resolution; therefore, QW thickness fluctuation is unlikely to be the main cause of collection. A weak photocurrent is also observed, and at the trap center, a broad ($\Delta E \approx$ 10 meV) low-intensity emission ~1.565 eV is seen. This signals the presence of local inhomogeneous fields and/or current flows. Using the PL from the heavily doped $n^+$-*GaAs* layer, we determined that the Fermi level lowered by ~1 meV at the trap center, which indicated a lighter local electron concentration that may be related to variation in doping and/or vacancies or a photogenerated carrier drain.

We have further investigated the electric field–dependent PL and the photocurrent characteristics of the samples under different excitation conditions: (i) various excitation energy (h$\nu$), (ii) different excitation spot sizes—uniform or localized (a spot of ~5- to ~10-μm diameter), and (iii) continuous wave (CW) or pulsed excitation. In the experiments presented thus far, e-h pairs are photogenerated uniformly over a large area by a HeNe laser at h$\nu$ = 1.96 eV, ~20 meV above the $Al_{0.33}Ga_{0.67}As$ barrier's bandgap ($E_{gb}$) (*28*). The effects reported above are readily observed for excitation energy h$\nu$ between $E_{gb}$ and $E_{ub}$ of ~2.34 eV. Note that they disappear sharply when h$\nu$ is tuned below $E_{gb}$ or above $E_{ub}$, even though the excitation is adjusted to create about the same density of e-h pairs in the CQWs. Moreover, when these effects are observed, the photocurrent-voltage characteristics of the sample show asymmetry with an N-shaped negative differential resistance (NDR) regime and photocurrent gain, signaling trapping of photogenerated carriers and/or buildup of space charges. Therefore, both the generation and transport of carrier in and/or across the AlGaAs barriers and the difference in carrier capture and/or escape by QWs are important for formation of the observed localized dense cold X systems.

Last, we performed two other sets of experiments: a comparison of $I_{PL}$ from the cloud

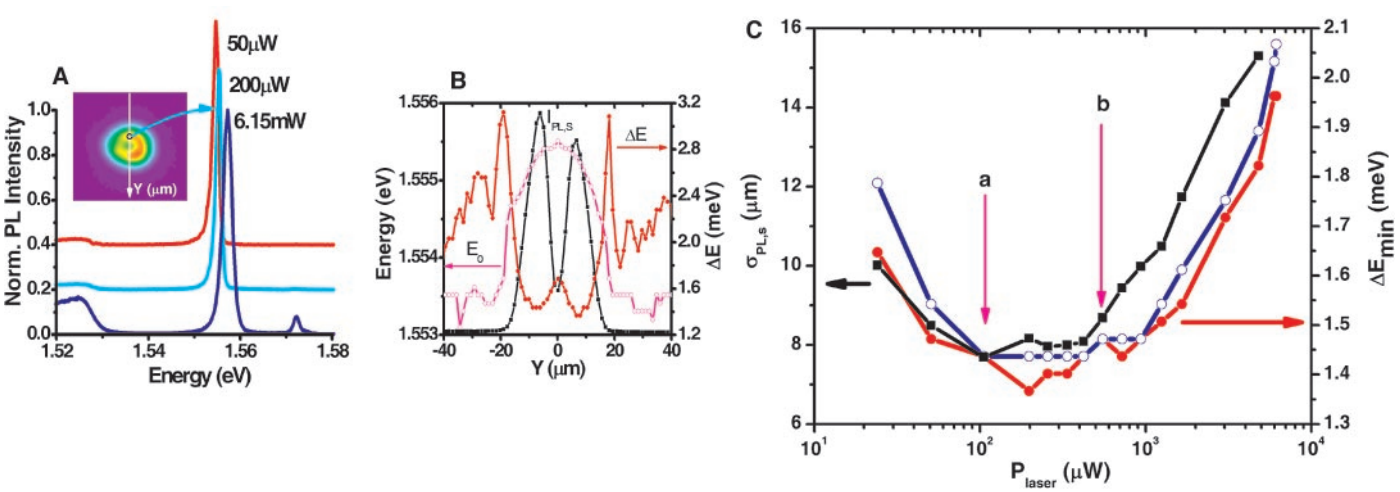


**Fig. 3.** Spatially resolved spectral analysis. (**A**) Selected PL spectra for $P_{laser}$ as indicated. The inset 2D PL image shows the path (white arrow) of a pinhole scanning across the trap to measure these spectra. The PL spectra shown are measured at the position (black circle) where the PL intensity is at a maximum. The spectra are normalized and vertically offset for clarity. The low-energy PL emission ($E < 1.53$ eV) is from $n^+$-GaAs layer, and the extra PL peak at $E = 1.572$ eV is from direct excitons. (**B**) Spatial profiles of spectrally integrated X PL ($I_{PL,S}$) (black curve), $\Delta E$ (red curve), and peak energy ($E_0$) obtained by analyzing scanned spectra at all positions for $T = 1.7$ K and $P_{laser} = 200$ μW. The locations of minimum linewidth ($\Delta E_{min}$) and maximum PL intensity coincide. (**C**) Two sets of $\Delta E_{min}$ values (blue and red curves) and cloud radii, $\sigma_{PL,S}$ (black curve), versus $P_{laser}$ at $T = 1.7$ K. The X-cloud radii are deduced from profiles of $I_{PL,S}$. The $\Delta E_{min}(P_{laser})$ and $\sigma_{PL,S}(P_{laser})$ curves have parallel variations, which reveal three regimes: (I) a dilute X system, (II) a degenerate condensed X fluid with narrowest $\Delta E_{min}$ and most concentrated cloud, and (III) a hybrid X/e-h phase. Arrows (a) and (b) indicate the approximate boundaries of regime (II), where the estimated maximum X density are (a) $1.7 \times 10^{10}$ and (b) $4.6 \times 10^{10}$ cm$^{-2}$, respectively.

Downloaded from www.sciencemag.org on January 8, 2008

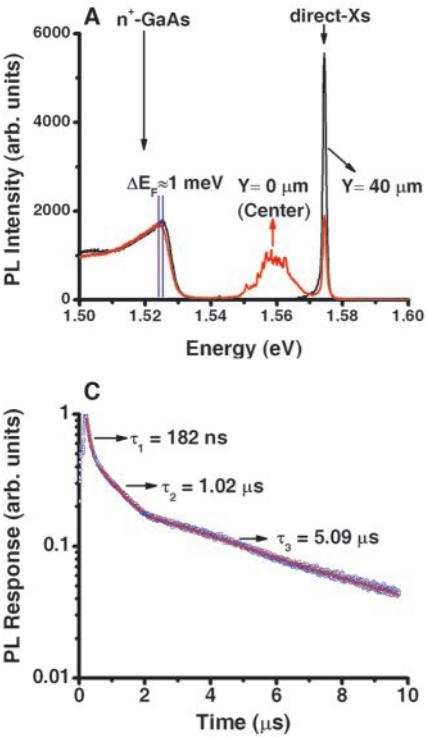


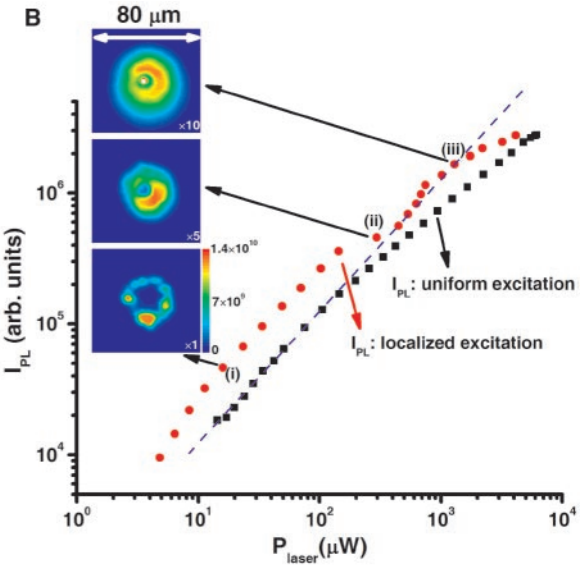


**Fig. 4.** (**A**) Spatially resolved spectra at the center of and 40 μm from the trap under zero applied electric fields. (**B**) Integrated PL ($I_{PL}$) with a uniform CW (black squares) and remote (~100 μm away) localized (red circles) HeNe excitation. The blue dashed line is a guidance of linear dependence. The inset PL images are taken with $P_{laser}$ = 15, 290, and 1100 μW. The color bar scale represents the estimated optically active X density for images scaled by ×1, ×5, and ×10 , respectively. (**C**) Dynamics of the PL from the indirect-X cloud measured with an ~20-ns pulsed localized (~10-μm diameter spot) excitation of hν = 1.95 eV 100 μm away. The laser has an average $P_{laser}$ = 26 μW and 100 kHz repetition rate. The PL exhibits a long decay that can be divided approximately into three stages with decay time τ ≈ 180 ns, 1 μs, and 5 μs. This signals a continuous formation of indirect Xs, because the lifetimes of indirect Xs are typically on the order of 100 ns only.

under uniform CW excitation and remote (~100 μm away) localized excitation, and transient measurements under remote, localized 10- to 20-ns pulsed excitation at hν = 1.95 eV. In the first case, shown in Fig. 4B, under uniform excitation, $I_{PL}$ varies approximately linearly with $P_{laser}$; whereas under remote localized excitation (see Fig. 4B, inset, X-cloud PL images), $I_{PL}$ first grows linearly and then exhibits a kink followed by a superlinear growth at $P_{laser}$ ≈ 200 μW. In the second case, the transient photocurrent response consists of a brief and intense pulse followed by a weak, steady long-lived (nearly 10-μs) component. Correspondingly, the PL dynamics (Fig. 4C) shows an extremely long decay time of the indirect Xs. These results imply that the indirect-X clouds are formed not only by the collection of photogenerated carriers, but also by a continuous formation of indirect Xs through photoinduced carrier transport and injection across the $n^+$-$i$-$n^+$ structure.

Putting all these observations together, we propose the following model: The localized dark spot at the center of the X cloud is associated with a pinhole that funnels a current filament through the $n^+$-$i$-$n^+$ structure. This source of current is smaller than or on the order of our spatial resolution of ~2 μm. In the absence of photoexcitation, it contributes only to the leakage current, but provides a localized source of majority carriers of one type. For low excitation density, corresponding to regime I, carriers of the opposite type flow toward the current source by the carrier imbalance mechanism proposed and modeled in (*29*, *30*). Indirect Xs are formed where the two types of carriers merge, which results in an extended indirect-X system. As the photoexcitation increases, at some point, both types of carriers are injected into CQWs, which results in an X density strongly peaked at center (Fig. 3B) and a concentrated cloud as shown in the central image of Fig. 1B. This corresponds to regime II. As the excitation density increases further to reach regime III, effects of the underlying Fermi statistics become apparent. The picture that has emerged is quite different from that of a condensation of Xs preexisting in the structure. Nevertheless, we have found conditions of temperature and photoexcitation that result in formation of highly statistically degenerate cold X systems where quantum mechanical collective effects can be observed. The insights gained in the formation mechanisms of the degenerate indirect X systems can lead to new strategies for producing confined cold X systems artificially in a more controllable way.

### References and Notes


1. E. A. Cornell, C. E. Wieman, *Rev. Mod. Phys.* **74**, 875 (2002).
2. W. Ketterle, *Rev. Mod. Phys.* **74**, 1131 (2002).
3. L. V. Keldysh, Y. V. Kopaev, *Soviet Phys. Solid State* **6**, 2219 (1965).
4. L. V. Keldysh, A. N. Kozlov, *Soviet Phys. JETP* **27**, 521 (1968).
5. L. V. Keldysh, in *Bose-Einstein Condensation*, A. Griffin, D. W. Snoke, S. Stringari, Eds. (Cambridge Univ. Press, Cambridge, 1995), pp. 246–280.
6. I. E. Perakis, *Nature* **417**, 33 (2002).
7. C. F. Klingshirn, in *Semiconductor Optics* (Springer-Verlag, New York, 1997), pp. 306–328.
8. C. D. Jeffries, L. V. Keldysh, Eds., *Electron-Hole Droplets in Semiconductors* (North-Holland, Amsterdam, 1983), pp. xxxvii, 656.
9. T. M. Rice, in *Solid State Physics—Advances in Research and Applications* (Academic Press, New York, 1977), vol. 32, pp. 1–86.
10. T. Fukuzawa, E. E. Mendez, J. M. Hong, *Phys. Rev. Lett.* **64**, 3066 (1990).
11. L. V. Butov, A. Imamoglu, A. V. Mintsev, K. L. Campman, A. C. Gossard, *Phys. Rev. B* **59**, 1625 (1999).
12. A. L. Ivanov, P. B. Littlewood, H. Haug, *Phys. Rev. B* **59**, 5032 (1999).
13. A. L. Ivanov, *Europhys. Lett.* **59**, 586 (2002).
14. P. C. Hohenberg, *Phys. Rev.* **158**, 383 (1967).
15. V. N. Popov, *Theor. Math. Phys.* **11**, 565 (1973).
16. V. Bagnato, D. Kleppner, *Phys. Rev. A.* **44**, 7439 (1991).
17. W. Ketterle, N. J. van Druten, *Phys. Rev. A.* **54**, 656 (1996).
18. Materials and methods are available as supporting material on *Science* Online.
19. L. V. Butov, C. W. Lai, A. L. Ivanov, A. C. Gossard, D. S. Chemla, *Nature* **417**, 47 (2002).
20. L. V. Butov, A. C. Gossard, D. S. Chemla, *Nature* **418**, 751 (2002).
21. D. Snoke, S. Denev, Y. Liu, L. Pfeiffer, K. West, *Nature* **418**, 754 (2002).
22. H. B. Bebb, E. W. Williams, in *Semiconductors and Semimetals*, R. K. Willardson, A. C. Beer, Eds. (Academic Press, New York, 1972), vol. 8, pp. 181–320.
23. J. Feldmann *et al.*, *Phys. Rev. Lett.* **59**, 2337 (1987).
24. X. J. Zhu, P. B. Littlewood, M. S. Hybertsen, T. M. Rice, *Phys. Rev. Lett.* **74**, 1633 (1995).
25. H. Reinholz, *Solid State Commun.* **123**, 489 (2002).
26. M. M. Dignam, J. E. Sipe, *Phys. Rev. B* **43**, 4084 (1991) and.
27. M. M. Dignam and J. E. Sipe, private communication.
28. S. Adachi, *GaAs and Related Materials: Bulk Semiconducting and Superlattice Properties* (World Scientific, River Edge, NJ, 1994), pp. xix, 675.
29. L. V. Butov *et al.*, arXiv: cond-mat/0308117.
30. R. Rapaport *et al.*, arXiv: cond-mat/0308150.


31. We thank L. V. Butov and D. H. Lee for fruitful discussions and K. L. Campman for growing the high-quality coupled quantum wells sample. This work is supported by the Office of Science, Office of Basic Energy Science, Division of Materials Sciences of the U.S. Department of Energy.


**Supporting Online Material**
www.sciencemag.org/cgi/content/full/303/5657/503/DC1
Materials and Methods
Fig. S1
Movie S1

17 October 2003; accepted 10 December 2003

Downloaded from www.sciencemag.org on January 8, 2008